

Point defect dynamics in bcc metals

Jörg Rottler, David J. Srolovitz, and Roberto Car

Princeton Institute for the Science and Technology of Materials (PRISM), Princeton University, Princeton, NJ 08544

(Dated: March 19, 2018)

We present an analysis of the time evolution of self-interstitial atom and vacancy (point defect) populations in pure bcc metals under constant irradiation flux conditions. Mean-field rate equations are developed in parallel to a kinetic Monte Carlo (kMC) model. When only considering the elementary processes of defect production, defect migration, recombination and absorption at sinks, the kMC model and rate equations are shown to be equivalent and the time evolution of the point defect populations is analyzed using simple scaling arguments. We show that the typically large mismatch of the rates of interstitial and vacancy migration in bcc metals can lead to a vacancy population that grows as the square root of time. The vacancy cluster size distribution under both irreversible and reversible attachment can be described by a simple exponential function. We also consider the effect of highly mobile interstitial clusters and apply the model with parameters appropriate for vanadium and α -iron.

PACS numbers: 61.80.Az, 61.82.Bg, 61.72.Cc

I. INTRODUCTION

Many properties of metals depend crucially on the type and concentration of defects that perturb the ideal crystal structure. Of these, the simplest are point defects, such as self-interstitials and vacancies. Since their formation energies are of order electron volts, their equilibrium concentrations tend to be very low. They do form in abundance, however, in radiation environments due to the collisions between the irradiating species (electrons, heavy ions or neutrons) and the atoms of the host crystal¹. When the energy of the impinging particle is close to, but above, the displacement threshold, the collision typically produces a single Frenkel pair. Particles with higher kinetic energy, for instance neutrons produced in fusion reactions, create collision cascades which can produce not only Frenkel pairs, but an ensemble of mobile and immobile self-interstitial and vacancy clusters of different sizes. The ensuing evolution of the point defect distributions due to diffusion² determines the long time scale degradation of the mechanical properties of the material, in addition to volume swelling at large doses.

For body centered cubic (bcc) metals, such as α -Fe, V and Mo, molecular dynamics simulations have revealed a detailed microscopic picture of the diffusive motion of individual defects and vacancies³. While the migration barrier ΔE_v for vacancy migration is rather high (~ 0.5 eV), both self-interstitial atoms and small self-interstitial cluster are highly mobile and easily diffuse along particular crystallographic directions ($\langle 111 \rangle$ -directions). In V, the lowest energy self-interstitial configuration is a $\langle 111 \rangle$ -oriented dumbbell, which migrates easily with a crowdion transition state⁴. However, this easy migration, with barriers as low as $\Delta E_i \sim 0.02$ eV⁵, leads to long one-dimensional self-interstitial diffusional trajectories. The self-interstitial dumbbell can change direction by rotating into other $\langle 111 \rangle$ -directions. The barrier associated with such rotations ΔE_r is of the same order as ΔE_v (i.e., $\Delta E_r \gg \Delta E_i$).

In α -Fe, by contrast, the ground state of the dumbbell self-interstitial is the $\langle 110 \rangle$ configuration, and accessing the easy-glide $\langle 111 \rangle$ configuration requires overcoming a qualitatively similar rotational barrier that separates the $\langle 110 \rangle$ from the $\langle 111 \rangle$ configurations⁶. Although the migration barriers for the crowdion mechanism in α -Fe are also believed to be very small (< 0.04 eV), the observed effective migration barrier (including rotation into the $\langle 111 \rangle$ orientation and migration along the $\langle 111 \rangle$ -direction) are higher than in V^{29,30}. Similar arguments apply to Mo and Ta. Both diffusion mechanisms imply that interstitial transport in bcc metals takes place in the form of long one-dimensional trajectories with occasional directional changes that become more frequent as the temperature increases. In fcc metals such as Cu, for instance, simulations showed that self-interstitial diffusion occurs through much more conventional, isotropic diffusion mechanisms²⁷. In most metals, however, large separations in time scale between self-interstitial and vacancy motion exist.

The intent of the present study is to illuminate the consequences of the intriguing microscopic diffusion mechanisms in bcc metals on the evolution of the point defect population using simple, but readily generalizable models. Our models shall minimally include local self-interstitial/vacancy mutual annihilation and absorption into (unsaturable) sinks which, in a real system, are in the forms of dislocations or grain boundaries. Together with the continuous production of point defects, these processes form the fundamental events in metals under irradiation conditions.

On the continuum level, point defect dynamics can be described by a set of kinetic master or rate equations that treat the point defects as a continuous density whose temporal evolution is governed by various gain and loss processes. These equations do not take into account spatial correlations and are only analytically tractable in the simplest situations. Although we focus the discussion specifically on bcc metals, the continuum theory makes

no reference to the underlying crystal structure and could be readily applied to fcc metals as well. In many cases, single interstitials and vacancies combine with defects of the same type to form stable clusters. The evolution of the cluster size distribution and other microscopic variables is more conveniently studied in a particle based model that explicitly represents defects and their diffusion mechanisms (translation, rotation) on a lattice. The competition of events occurring with different rates can then be followed using a kinetic Monte Carlo (kMC) scheme.

Both master equation and Monte Carlo approaches have frequently been employed to illuminate the physics of damage evolution in irradiated materials. Starting from the elementary processes mentioned above⁷, steady-state rate equations have been used to study the effects of preferential absorption of self-interstitial atoms at sinks (absorption bias)^{8,9}, the formation of interstitial cluster during the cascade phase (production bias)^{8,9,10,11}, and the one-dimensional motion of these clusters in bcc metals^{9,10,11}. kMC models were first used to evolve the primary damage state obtained from ns-long MD simulations to macroscopic time scales, but have increasingly been used to study the evolution of defect structure during continuous irradiation in copper^{12,13,14}, vanadium¹⁵ and iron¹⁶.

Although many treatments have included a high level of atomistic detail from the start, we begin by analyzing the simplest situation that includes only production of Frenkel pairs, point defect recombination and absorption at sinks in Section II. Even though this simplified case has been studied many times before⁷, we shall see that the inclusion of specific features of bcc metals leads to a surprisingly rich evolutionary picture. This approach allows us to gradually increase the level of complexity of the model in a verifiable, controlled manner. We introduce first interactions between vacancies that lead to vacancy cluster formation in Section III and then interactions between interstitials in Section IV. In particular, we shall discuss how interstitial cluster mobility affects vacancy cluster formation. While the discussion in the text is applicable to bcc metals broadly, we apply our findings to the specific cases of V and α -Fe in Section V.

II. POINT DEFECT DYNAMICS IN SIMPLE SITUATIONS

A. Atomistic details and kMC model

The physics of radiation damage evolution is governed by the production of defects due to irradiation and their subsequent elimination from the population through diffusional processes. Typical values for the defect production rate σF range between 10^{-3} dpa/s, in ion irradiation experiments¹⁷, and 10^{-10} dpa/s, for neutron irradiation¹⁴, where F is the irradiation flux and σ is the cross-section. A “displacement per atom” (dpa) refers to

the production of one Frenkel defect pair per lattice site.

Self-interstitial transport is composed of two parts, a one-dimensional diffusive motion along one of the 4 distinct $\langle 111 \rangle$ directions and dumbbell rotations from one $\langle 111 \rangle$ direction to another. The temperature dependence of the (one-dimensional) diffusivity D_i is usually described through the Arrhenius form in most cases except for vanadium, where the unusually low activation barrier can lead to more complicated behavior at higher T (see Ref. 5). For $T < 600K$, however, the interstitial diffusivity is well described by the Arrhenius expression $D_i/a^2 = f\nu_i \exp[-\Delta E_i/k_B T]$, where ΔE_i is the activation energy barrier, ν_i an attempt frequency and correlations are expressed through the correlation factor f ($f = 1$ when the diffusion is uncorrelated). The temperature dependence of the rotation rate γ_r , by contrast, is always of the Arrhenius form, $\gamma_r = \nu_r \exp[-\Delta E_r/k_B T]$, where ΔE_r the characteristic rotation barrier and ν_r is an attempt frequency. Values for both ν_i and ν_r range between $10^{12}s^{-1}$ and $10^{13}s^{-1}$. Finally, vacancies diffuse three-dimensionally with rate $D_v/a^2 = \nu_v \exp[-\Delta E_v/k_B T]$, where ΔE_v and ν_v are the activation barriers and attempt frequencies, respectively. The defects can undergo two basic reactions: recombination once an interstitial and vacancy defect are within a certain “recombination volume”, or absorption at sinks. Typical dislocation densities in metals are of the order $10^{12} - 10^{14} m^{-2}$, which translates into dislocation sink densities (per lattice site) of $n_s \sim 10^{-4} - 10^{-6}$.

Since the relevant time scales (ns-sec) for the evolution of the point defect distributions far exceed those of molecular dynamics simulations, we employ a coarse grained description, in which we represent vacancies, dumbbell interstitial configurations and sinks as pointlike objects that occupy ideal lattice sites of a bcc lattice with lattice parameter a . In order to mimic constant irradiation conditions, new pairs of defects (self-interstitial and vacancy) are introduced randomly onto defect-free lattice sites with rate σF . The microscopic diffusion process is replaced by instantaneous hops of point defects to vacant neighboring lattice sites with rates D_i/a^2 and D_v/a^2 , respectively. A self-interstitial is constrained to forward-backward hops along one of the four $\langle 111 \rangle$ directions, but can also rotate to another $\langle 111 \rangle$ direction with rate γ_r . Vacancies diffuse isotropically. A self-interstitial or vacancy recombines if it finds itself next to a vacancy or self-interstitial, respectively, or is absorbed if one of its 8 neighboring sites contains a sink. At each time step, an event is chosen according to its probability and then executed. Time is advanced according to the usual continuous time algorithm¹⁸, where the time increment is chosen from an exponential distribution.

B. Basic rate equations

The elementary processes described in the kMC model can, alternatively, be described within a rate equation

formalism. Before the advent of large scale computer simulations, this method represented the only viable theoretical approach for simulating long time radiation damage evolution. The rate equations can be solved by direct numerical integration or direct analysis in limiting cases. In the minimal model discussed above, the time evolution of the number densities of the interstitials $n_i(t)$ and vacancies $n_v(t)$ is given by the coupled nonlinear equations^{7,19,23}

$$\begin{aligned}\frac{dn_i}{dt} &= \sigma F - \kappa_v \omega_{iv} n_i - \kappa_i \omega_{vi} n_v - \kappa_{is} \omega_{is} n_i \\ \frac{dn_v}{dt} &= \sigma F - \kappa_v \omega_{iv} n_i - \kappa_i \omega_{vi} n_v - \kappa_{vs} \omega_{vs} n_v\end{aligned}\quad (1)$$

Defect pairs are added to the population at a rate proportional to the particle flux F and a cross-section σ . Loss can occur through a diffusing interstitial recombining with a vacancy with rate ω_{iv} and a diffusing vacancy recombining with an interstitial with rate ω_{vi} . The recombination rates are all proportional to the diffusion constant of the moving defect, but depend on the dimensionality of the diffusion process. κ_i and κ_v are dimensionless capture numbers that represent the spatial extent of the defects and their effective (possibly long ranged) interactions. Losses can also occur through absorption at sinks with rates ω_{is} and ω_{vs} and corresponding capture numbers κ_{is} and κ_{iv} for interstitials and vacancies, respectively. An alternative representation of Eqs. (1) is to define sink strengths k_x^2 via the relation $k_x^2 D_x = \kappa_x \omega_x$, where the subscript x refers to any of the combination of indices used above.

The encounter rates of the defects are given by the number of distinct sites visited by a random walker per unit time. Since the mean squared displacement $\langle R^2 \rangle = l^2 N$ for a random walk with step length l , the number of sites visited is $s = [\langle R^2 \rangle / l^2]^{1/2} \sim N^{1/2}$ in one dimension. By contrast, a detailed analysis of random walks on three-dimensional cubic lattices shows that a random walker visits $\mathcal{O}(N)$ distinct sites after N hops. For a given density of target sites n , the typical collision time τ_c is given by the condition $D\tau_c/a^2 = 1/n$ (3D) and $(D\tau_c/a^2)^{1/2} = 1/n$ (1D), from which we deduce the encounter rates

$$\omega_{3D} \sim nD/a^2 \quad \text{and} \quad \omega_{1D} \sim n^2 D/a^2. \quad (2)$$

In a similar manner, the capture numbers κ are also affected by the dimensionality of the random walk. Assuming ideal spherical defects of linear dimension r , $\kappa \sim r/a$ for a 3D random walk in a mean-field approximation²⁰, but in general, capture numbers can also depend on spatial fluctuations and dose. For a 1D random walk, the scaling with defect size becomes much stronger²¹, $\kappa \sim (r/a)^4$.

These expressions apply to strictly 1D or 3D random walks. As discussed in the Introduction, we encounter an intermediate case in bcc metals, where rotations interrupt 1D random walks and lead to 3D trajectories.

The encounter rate of this random walk must, therefore, be larger than the purely 1D case. For a rotation rate γ_r , the random walker performs on average $D/\gamma_r a^2$ hops along a particular direction before rotating into a new direction. There are $\gamma_r \tau$ of these segments during time τ . The mixed 1D/3D collision time thus follows from the condition $(D/\gamma_r a^2)^{1/2} \gamma_r \tau_c = 1/n$, which implies

$$\omega_{1D/3D} = \omega_{3D} \sqrt{\gamma_r a^2 / D} \quad (3)$$

The mixed encounter rate $\omega_{1D/3D}$ scales like the 3D encounter rate ω_{3D} , but is reduced by the square root of the ratio of the number of rotations to hops. This reaction rate has also been derived in ref. 21. This work views the kinetics in the intermediate 1D/3D regime as an enhanced 1D reaction rate, but the resulting expressions agree up to numerical prefactors. These authors also showed that the size dependence of the mixed capture number $\kappa \sim (r/a)^2$, and ref. 22 provides an interpolation formula between the limiting cases using a continuum description. While the encounter rates and reaction kinetics of random walkers decrease when the dimensionality of the random walk changes from three to one, the diffusivity does not, since the mean squared displacement of a random walk of N steps of length l is $\langle \mathbf{R}(N)^2 \rangle = l^2 N$ independent of dimensionality.

Note that these encounter rates are derived under the assumption of collisions with a stationary target. The case of several colliding 1D random walkers becomes equivalent to a 3D random walk because, from the rest frame of a given walker, the other walkers appear to be executing a 3D random walk. This case would be relevant for describing the collisions of interstitials with each other, but not with the vacancies or sinks.

Inserting these encounter rates into Eqs. (1), assuming mixed 1D/3D encounter for diffusing interstitials, yields rate equations of the form

$$\begin{aligned}\frac{dn_i}{dt} &= \sigma F - n_i n_v (\kappa_v \sqrt{\beta} D_i / a^2 - \kappa_i D_v / a^2) \\ &\quad - \kappa_{is} n_s n_i \sqrt{\beta} D_i / a^2\end{aligned}\quad (4)$$

$$\begin{aligned}\frac{dn_v}{dt} &= \sigma F - n_i n_v (\kappa_v \sqrt{\beta} D_i / a^2 - \kappa_i D_v / a^2) \\ &\quad - \kappa_{vs} n_s n_v D_v / a^2,\end{aligned}\quad (5)$$

where $\beta = \gamma_r a^2 / D_i$ is a dimensionless ratio that describes the relative frequency of dumbbell rotations and diffusional hops.

C. Simple scaling analysis

We now specialize these results to the common case of bcc metals, where $\gamma_r a^2 / D_i \ll 1$ and $D_i / D_v \gg 1$. Before performing the kMC simulations and solving the full rate equations numerically, it is instructive to analyse the limiting behaviors of this system²³. Initially, there are no defects in the metal, and only the first term in the

rate equations is important. In this regime (regime I), defect densities increase linearly with time,

$$n_i^I = n_v^I = \sigma F t. \quad (6)$$

Once a sufficient density of defects has been produced such that the encounter times between defects becomes smaller than the time between creation events, loss through recombination (2^{nd} and 3^{rd} terms) becomes important²⁴. As we shall see below, typical parameter ranges lead to a situation in which defect recombination becomes important before sink loss. The balance between creation and recombination makes a steady state possible: $dn_i/dt = dn_v/dt = 0$. Ignoring the sink terms, one readily finds for this Regime II

$$n_i^{II} = n_v^{II} = \left(\frac{\kappa_v \sqrt{\beta} D_i + \kappa_i D_v}{\sigma F a^2} \right)^{-1/2} \sim \Gamma^{-1/2}, \quad (7)$$

which only depends on the dimensionless ratio $\Gamma = \frac{(\sqrt{\beta} D_i + D_v)}{\sigma F a^2}$. The crossover from Regime I to Regime II occurs at time $t_{I/II} = F \sigma t_{I/II} \simeq \Gamma^{-1/2}$, i.e., $t_{I/II} \sim n_i^{-1} (D_i/a^2)^{-1}$. Note that this scaling regime is bound from above by the following condition: if n_v becomes so large that the time between interstitial-vacancy encounters is on average shorter than the time between two subsequent rotations (i.e., if $\Gamma < \beta^{-1}$), the scaling of the encounter time becomes that of a 1D random walk. In this case, the scaling of the steady state defect density with Γ changes from $n_i^{II} = n_v^{II} \sim \Gamma^{-1/2}$ to $n_i^{II} = n_v^{II} \sim \Gamma^{-1/3}$. This regime is unlikely to be of experimental relevance.

Eventually, loss through sinks becomes important and the steady state Regime II ends. Clearly, there exists a terminal steady state (see below) in which all loss terms in Eqs. (1) balance the creation of defects. If $D_i \gg D_v$ as in the bcc metal case, however, the system will initially lose mostly interstitials and very few vacancies. This breaks the symmetry between interstitials and vacancies and $n_v \gg n_i$. The second steady state is, therefore, reached through a transient Regime III with distinct scaling. Subtracting the two rate equations (and neglecting vacancy loss at sinks),

$$\frac{d(n_v - n_i)}{dt} \simeq \frac{dn_v}{dt} = \kappa_{is} n_s \sqrt{\beta} \frac{D_i}{a^2} n_i, \quad (8)$$

where n_s denotes the sink density. This equation allows us to eliminate n_i in the rate equation for n_v , so that

$$\frac{dn_v}{dt} \simeq \sigma F - \frac{\kappa_v n_v}{\kappa_{is} n_s} \frac{dn_v}{dt}. \quad (9)$$

Integrating Eq. (9), we obtain (to leading order) power-law growth of n_v with time,

$$n_v^{III} \simeq (\kappa_s n_{is} \sigma F t / \kappa_v)^{1/2}. \quad (10)$$

In the case of extremely large sink densities n_s , the encounter rates ω_{is} between interstitials and sinks would not be 3D as assumed above, but 1D-like. In this case,

n_s would have to be replaced by n_s^2 , but again, such high densities are unrealistic. The crossover time $t_{II/III}$ between Regimes II and III can be obtained from the condition $\Gamma \simeq \kappa_{is} n_s \sigma F t_{II/III} / \kappa_v$, which implies $t_{II/III} \sim (\kappa_v / \kappa_{is} n_s)^{1/2} / (D_i/a^2)$. The crossover occurs at constant time, independent of the defect densities.

If there are only sinks for one species of defect and no sinks for the other, Regime III will simply continue. In all other cases, a final steady state will occur when all loss terms are important. Setting again $\frac{dn_i}{dt} = \frac{dn_v}{dt} = 0$ as in Ref. 19, we obtain a condition for steady state,

$$\frac{n_v^{IV}}{n_i^{IV}} = \frac{\sqrt{\beta} D_i}{D_v} = \frac{\kappa_{is}}{\kappa_{vs}} \alpha \sqrt{\beta}, \quad (11)$$

where we have introduced a third dimensionless ratio $\alpha = D_i/D_v$. The interstitial and vacancy populations will, in general, be different. The steady state values are the roots of the quadratic equation

$$(n_v^{IV})^2 \frac{\kappa_{vs} \Gamma}{\kappa_{is} \alpha \sqrt{\beta}} - n_v^{IV} \frac{\kappa_{vs} n_s D_v}{\sigma F a^2} = 1. \quad (12)$$

Since typically $n_s \ll 1$, the linear term can be neglected relative to the quadratic term, and we obtain the scaling of the vacancy density in Regime IV,

$$n_v^{IV} \sim \left(\frac{\Gamma}{\alpha \sqrt{\beta}} \right)^{-1/2}. \quad (13)$$

The crossover time $t_{III/IV}$ follows again from the condition $\kappa_{is} n_s \sigma F t_{III/IV} / \kappa_v \simeq (\Gamma / \alpha \sqrt{\beta})^{-1}$, i.e., $t_{III/IV} \sim (\alpha \sqrt{\beta} \kappa_v / \kappa_{is} n_s)^{1/2} / (D_i/a^2)$ is again independent of n_i or n_v .

The volume swelling is proportional to the excess vacancy population in this regime, $S = n_v - n_i$. Note that the imbalance arises here due to the very different diffusivities of the two types of defects. Upon termination of the irradiation, both the n_i - and n_v -populations would relax exponentially to zero in this simple model.

D. Numerical integration and kMC

A full solution of the rate equations (1) is only possible numerically. In the following, we show a series of such numerical and kinetic Monte Carlo simulation results for a representative choice of parameters $D_i = 1000 D_v$, $\gamma_r = 0.01 D_i/a^2$, so that $\alpha = 1000$ and $\beta = 0.01$ (see Section V for typical experimental regimes). In addition, we set the density of sinks to $n_s = 10^{-4}$. Figure 1 shows the evolution of the average interstitial and vacancy density (symbols) based on the above parameters obtained from the kMC simulation and numerical integration of the corresponding rate equations (solid lines) using the expression Eq. (3) for the mixed encounter rates. The dimensionless parameter Γ was varied by changing the defect creation rate $F \sigma$. As predicted by the scaling analysis, four distinct regimes appear with increasing time.

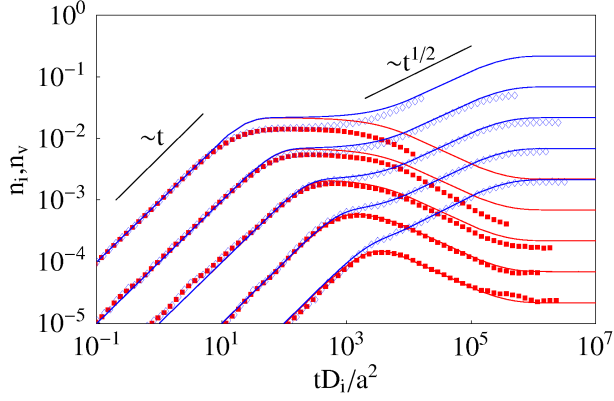


FIG. 1: Self-interstitial (\blacksquare), n_i , and vacancy (\diamond), n_v , densities as a function of time for $\Gamma = 10^2, 10^3, 10^4, 10^5$, and 10^6 (Γ increases from the top to bottom of the figure). Time is measured in units of the inverse interstitial hopping rate a^2/D_i . The solid lines show the result of direct numerical integration of Eqs. (1) with $\kappa_v = \kappa_i = \kappa_{is} = \kappa_{vs} = 21$, and the symbols correspond to the results of the kMC simulations in a periodic simulation box. The straight solid lines have slope 1 and $1/2$.

After first rising linearly with time (Regime I), n_i and n_v reach the steady state plateau of Regime II. Once loss through sinks becomes important (Regime III), n_v increases as $t^{1/2}$ while n_i decreases. Finally, all curves reach the steady-state Regime IV, where n_i and n_v are given by Eqs. (11) and (12). At the highest defect densities, the kMC simulations were not carried out into the final steady state regimes, because the computational effort becomes very large.

Excellent agreement between continuum theory and kMC model for the 3 largest values of Γ is achieved by adjusting all capture numbers to a single numerical constant. In the simple situation examined here, kMC and rate theory are completely equivalent. Since we have used $\omega_{1D/3D}$ in the rate equations, this agreement also validates the scaling argument for the mixed 1D/3D encounter rate. For the two smallest Γ -values, we observe increasing discrepancies between rate equations and kMC. As discussed above, we expect a transition from the mixed 1D/3D encounter rates ω_{iv} to 1D dominated encounter kinetics when the interstitial density becomes so high that they typically collide with vacancies or sinks before rotating ($\Gamma < 100$). This transition is not faithfully reproduced by the rate theory which assumes only the limiting cases of either 1D or mixed 1D/3D encounter rate scaling, but is properly captured by the kMC which includes explicit 1D/3D trajectories.

Note also that with increasing Γ , Regime II begins to shrink and Regime I crosses over directly into Regime III. This happens because as the defect densities decrease below the sink density, point defect loss at sinks will become dominant before recombination plays a significant role. Since the crossover time $t_{I/III} \simeq \kappa_s n_s / \kappa_v \sigma F$ only depends on the point defect production rate, a further decrease of the production rate will eventually lead to a

direct crossover from Regime I to Regime IV. A smaller sink density would push the appearance of Regimes II and III to higher values of Γ .

III. VACANCY CLUSTER FORMATION

A. Irreversible aggregation

To this point, neglected interactions between vacancies. Experimental vacancy-vacancy binding energies E_b can be of order the single vacancy migration energy. This suggests that it is not unreasonable to expect vacancies to form stable clusters or microvoids once they meet. A relatively simple approximation for this situation is to consider the limiting case of “irreversible aggregation”, which neglects any dissociation of a vacancy from a cluster and thus sets $E_b = \infty$. The realistic situation, which includes finite binding energies, can be viewed as an intermediate case between irreversible aggregation and the case of $E_b = 0$ of the previous section.

In the “irreversible aggregation” model, vacancies bind to form stable divacancies, leaving the population of free vacancies, while interstitials recombining with a divacancy recreate a single mobile vacancy. Stable cluster grow or shrink under the influence of arriving vacancies and interstitials. Denoting the number density of clusters of size m as $n_c(m)$, we can write the following set of rate equations²⁵:

$$\begin{aligned}
 \frac{dn_i}{dt} &= \sigma F - \kappa_i \omega_{vi} n_v \\
 &\quad - (\kappa_v \omega_{iv} + \kappa_{is} \omega_{is} + \sum_m \kappa_i^m \omega_{ic(m)}) n_i \\
 \frac{dn_v}{dt} &= \sigma F - (\kappa_i \omega_{vi} + \kappa_{vs} \omega_{vs} + \sum_m \kappa_v^m \omega_{vc(m)}) \\
 &\quad - 2\kappa_v \omega_{vv} n_v - (\kappa_v \omega_{iv} - \kappa_i^2 \omega_{is(2)}) n_i \\
 \frac{dn_c(m)}{dt} &= (\kappa_v^{m-1} \omega_{vc(m-1)} - \kappa_v^m \omega_{vc(m)}) n_v \\
 &\quad + (\kappa_i^{m+1} \omega_{ic(m+1)} - \kappa_i^m \omega_{ic(m)}) n_i, \quad (14)
 \end{aligned}$$

where $n_v \equiv n_c(1)$ is now understood to refer to the free vacancy density (or cluster of size 1). The additional terms in the equations for the evolution of n_i and n_v account for interstitial/vacancy-cluster encounters, vacancy/vacancy-cluster encounters, vacancy-cluster nucleation and divacancy decomposition. $\omega_{ic(m)} = n_c(m) \sqrt{\beta} D_i / a^2$, $\omega_{vc(m)} = n_c(m) D_v / a^2$ and $\omega_{vv} = n_v D_v / a^2$ denote the corresponding encounter rates. The last expression in (14) describes the evolution of stable, immobile vacancy clusters of size $m > 1$ due to the diffusive arrival of interstitials and vacancies. The hierarchy of rate equations (14) is, in principle, amenable to a semi-analytical treatment via numerical integration, if all constants κ_i^m / κ_v are specified. However, such a solution requires termination of the set of equations at a finite

cluster size m_{max} , i.e., one imposes a boundary condition $n_c(m_{max}) = 0$. The corresponding kMC model does not require any ad hoc assumptions and takes all these processes naturally into account.

Before examining this model in kMC, we can draw some preliminary conclusions. In Regime I, only nucleation of divacancies will be important. Since here the vacancy density grows linearly with time, we predict the scaling regime

$$n_c(2)^I \sim (\sigma Ft)^3. \quad (15)$$

The divacancy density grows cubically with time. In the steady-state Regime II, the vacancy cluster density is slaved to the free vacancy density and, therefore, is constant as well. For $\alpha \gg 1$, we expect the total cluster density $n_c = \sum_m n_c(m)$ to be much smaller than n_v and n_i , so that the presence of vacancy clustering does not yet strongly alter the interstitial and vacancy population. Using Eq. (7), we find

$$n_c^{II} \simeq \Gamma^{-1/2}/(\alpha\sqrt{\beta}). \quad (16)$$

Once past Regime II, the cluster density will begin to rise again as n_v increases. n_v will then increasingly fall below the total number of vacancies in the system n_{vtot} , because increasing numbers of vacancies $\sum_{m>1} mn_c(m)$ become immobilized in clusters. These clusters act as additional sinks for the diffusing vacancies, but do not remove them from the system. The higher the cluster density, the smaller the loss of vacancies through sinks and interstitial recombination. We therefore expect that Regime III will extend to larger times and the presence of the immobile vacancy cluster delays the onset of the final steady-state Regime IV.

For the total number of vacancies n_{vtot} , we can write the rate equations as

$$\begin{aligned} \frac{dn_{vtot}}{dt} &= \sigma F - \kappa_i \omega_{vi} n_v - \sum_{m=1} \kappa_i^m \omega_{ic(m)} n_i \\ \frac{dn_i}{dt} &= \sigma F - \kappa_i \omega_{vi} n_v - \left(\sum_{m=1} \kappa_i^m \omega_{ic(m)} - \kappa_{is} \omega_{is} \right) n_i, \end{aligned} \quad (17)$$

where we have neglected vacancy loss at sinks. This is the Regime III situation discussed earlier. Subtraction of Eqs. (17) and elimination of n_i , as in Eq. (9), leads to

$$\frac{dn_{vtot}}{dt} \simeq \sigma F - \frac{\kappa_v}{\kappa_{is} n_s} \frac{dn_{vtot}}{dt} \sum_{m=1} \frac{\kappa_i^m}{\kappa_v} n_c(m). \quad (18)$$

At relatively early times, when only small clusters are present, $\sum_{m=1} \frac{\kappa_i^m}{\kappa_v} n_c(m) \simeq n_{vtot}$ and n_{vtot} will initially increase as $n_{vtot} \sim (\kappa_{is} n_s \sigma F t)^{1/2}$. The subsequent behavior depends on the detailed form of the capture numbers κ_{is} .

In the absence of vacancy clustering, Regime III ends when the vacancy density has become so large that vacancy loss through sinks balances interstitial loss through

sinks. This condition, Eq. (11), must hold for a final steady state to appear. In the present simple model, this condition depends only on the ratio of the diffusivities, but in a real system, Eq. (11) also depends on sink concentrations and capture numbers, which may be different for interstitial and vacancies. Eventually this condition can also occur as a result of vacancy clustering, because vacancy clusters act as additional sinks for the interstitials and remove them symmetrically from the system. At high cluster densities, the low mobile vacancy concentration can therefore be compensated. In the steady-state regime IV, we expect the hierarchy $n_i^{IV} < n_v^{IV} < n_c^{IV} < n_{vtot}^{IV}$. Because of the later entry into Regime IV, $S = n_{vtot} - n_i$ (the total amount of volume swelling) will be larger than in the absence of clustering.

In Regime IV, we can obtain an approximate scaling relation for the total cluster density. The density is determined by the competition between nucleation of clusters out of the vacancy gas and decomposition of divacancies due to arriving interstitials. Denoting the fraction of clusters that represent divacancies as f , we can write the rate equation

$$\frac{dnc^{IV}}{dt} = \kappa_v n_v^2 D_v / a^2 - f(t) \kappa_i^2 n_c^{IV} n_i \sqrt{\beta} D_i / a^2, \quad (19)$$

which implies $n_c^{IV} = \kappa_v n_v^2 / f \kappa_i^2 \alpha \sqrt{\beta} n_i = \kappa_v n_v / f \kappa_2$, where we have used Eq. (11). The cluster density is therefore of order the free vacancy density with a numerical prefactor that depends on the mean cluster size.

1. Average cluster density

The effect of irreversible vacancy aggregation on the defect dynamics as seen through kMC is shown in Fig. 2 for three values of $\Gamma = 10^5$, $\Gamma = 10^7$ and $\Gamma = 10^9$ with all other parameters as before. In this figure, we also plot the total cluster density n_c and the total vacancy density n_{vtot} . In Regimes I and II, n_c and n_i are nearly unchanged. The defect density n_c rises first $\sim t^3$ and then remains constant during Regime II as discussed above. In Regime III, n_v begins to fall below the result from Fig. 1 because of trapping of vacancies into clusters. At the same time, n_{vtot} rises with an ideal $t^{1/2}$ law, and Regime III extends to larger times. n_c also rises again due to new cluster nucleation events out of the vacancy gas. All quantities reach constant values in regime IV. As one might expect, the total number of vacancies in the system is higher than in the absence of clustering. However, the general sequence of regimes remains unchanged.

In order to gain additional insight into the growth dynamics, we also numerically integrate the full set of rate Eqs. (14) (solid lines in Fig. 2). This requires specification of the capture numbers κ^m . In the simplest mean field model for nucleation dynamics, the capture numbers do not depend on cluster size m and $\kappa_{i,v}^1 = \kappa_{i,v}^m = \text{const.}$ (i.e., the point cluster model). Interestingly, we find

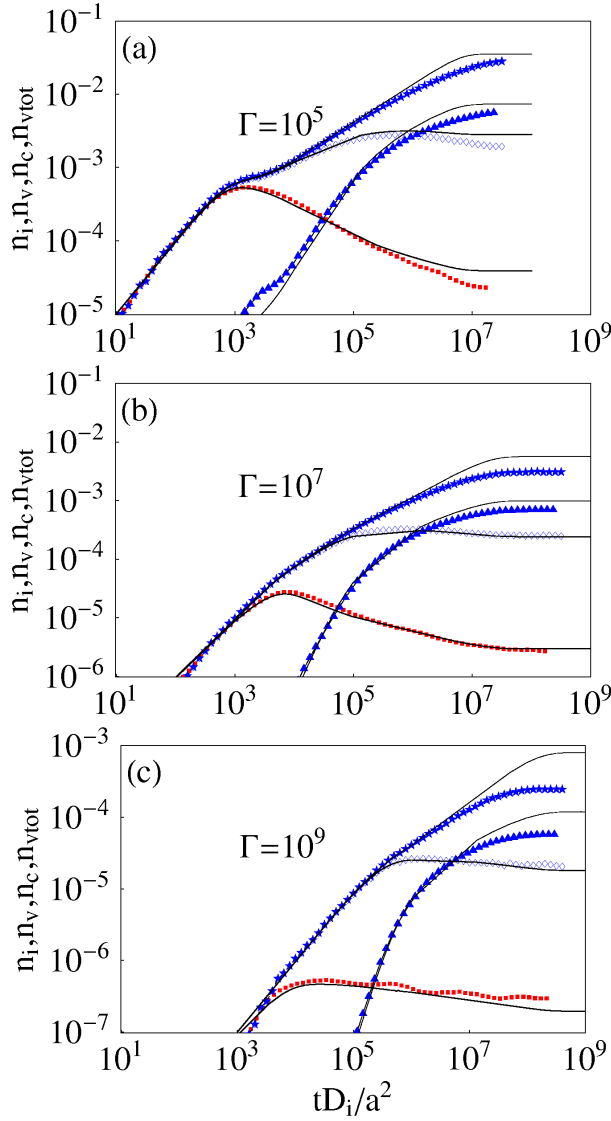


FIG. 2: Interstitial densities n_i (■), free vacancy density n_v (◇) as well as the total vacancy density n_{vtot} (★) and vacancy cluster density n_c (▲) as a function of time for (a) $\Gamma = 10^5$, (b) $\Gamma = 10^7$, and (c) $\Gamma = 10^9$. The thin solid lines show the result of direct numerical integration of Eqs. (14) with $\kappa_i^m = \kappa_v^m = 25$ and a $m_{max} = 20$ (see text).

surprisingly good agreement between the rate equations (solid lines in Fig. 2) and the full kMC simulations when using this simple approximation. This suggests that for relatively small m , κ^m is only very weakly size-dependent. The rate equations faithfully reproduce the sequence of regimes, but begin to show deviations at late times when larger clusters become more prominent and the point cluster assumption is no longer accurate. Here, κ^m begins to show some size dependence. The success of this comparison shows, however, that a mapping between kMC and rate equations is possible even with void nucleation and growth if the κ^m 's are accurately parametrized.

Note that in the present model, the volume swelling

rate dS/dt is zero in Regime IV. This is possible because we have chosen the same capture radii κ_s for the sinks for both interstitials and vacancies, i.e., the sinks are symmetric with respect to defect type. $S \sim t$ would be valid, if, for example, the capture radius for interstitials is larger than that for vacancies. This situation can arise with the introduction of dislocation sinks (known as “dislocation bias”) and has been invoked to explain unusually large swelling rates (see also Section VI) at times later than considered here^{8,9}.

2. Cluster size distribution

A full description of the evolution of the point defects in the material includes a characterization of the cluster size distribution. The growth of these clusters is the result of the diffusive arrival of interstitial and vacancy defects at already nucleated clusters. The full dynamics of this process is described by the last equation in (14). Consider this equation in the following simplified notation:

$$\frac{dn_c(m)}{dt} = n_v(\kappa_v^{m-1}n_c(m-1) - \kappa_v^m n_c(m))D_v/a^2 + n_i(\kappa_i^{m+1}n_c(m+1) - \kappa_i^m n_c(m))\sqrt{\beta}D_i/(i20)$$

If n_i and n_v change very slowly in time, the distribution $n_c(m)$ is given by the steady state solution to Eq. (20), i.e., $dn_c(m)/dt = 0$. This equation is supplemented by the detailed balance condition

$$n_v\kappa_v^m n_c(m)D_v/a^2 = n_i\kappa_i^{m+1}n_c(m+1)\sqrt{\beta}D_i/a^2, \quad (21)$$

which should also hold for $m \geq 2$. From this condition, we can deduce the distribution $n_c(m)$ by induction. Since $n_v \equiv n_c(1)$, we have $n_c(2) = n_v^2\kappa_1/(\kappa_i^2\alpha\sqrt{\beta}n_i)$ and consequently for all $m > 1$

$$n_c(m) = \frac{n_v^m}{(\alpha\sqrt{\beta}n_i)^{m-1}} \frac{\prod_{l=1}^{m-1} \kappa_v^l}{\prod_{l=2}^m \kappa_i^l}. \quad (22)$$

Equation (22) is tested against the kMC results in Fig. 3, where we show the cluster size distributions at four different times. All curves fall along straight lines in a semilogarithmic plot, and the slope decreases with increasing mean cluster size. A comparison with Eq. (22) requires, again, knowledge of the capture numbers κ^m . As in the previous section, use of the point cluster approximation $\kappa_{i,v}^l/\kappa_{i,v}^1 = 1$ yields excellent agreement between the kMC data and Eq. (22) upon inserting the values for $n_i(t)$ and $n_v(t)$ at the appropriate times.

Note that the distributions shown in Fig. 3 are not peaked, i.e., the frequency with which different clusters appear decrease with increasing cluster size and single vacancies occur most frequently. This situation is in sharp contrast to other cluster growth situations as, e.g., found in submonolayer island growth during vapor deposition²⁶, where the distribution $n_c(m)$ peaks at the

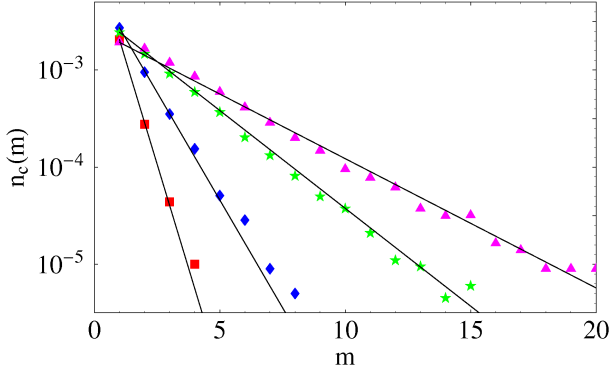


FIG. 3: Plot of the cluster size distribution $n_c(m)$ found from the kMC simulations with $\Gamma = 10^5$ of Fig. 2(a) at four different times $tD_i/a^2 = 3 \times 10^4$ (■), 3×10^5 (◆), 3×10^6 (★), and 3×10^7 (▲) in Regimes III and IV. The straight lines correspond to $n_v(t)^m / (\alpha\sqrt{\beta}n_i(t))^{m-1}$.

mean cluster size $\langle m \rangle$. In this problem, however, clusters cannot shrink, since vacancies are absent. One expects Eq. (22) to hold as long as the assumption of quasi-stationary values for n_i and n_v is valid.

B. Reversible attachment

The above discussion immediately raises the question of whether the results for $n_c(t)$ and its size distribution Eq. (22) survive in the more realistic situation of reversible cluster growth, i.e., vacancies have a finite probability to attach to and to leave the cluster. Let us introduce “detachment rates” from a cluster of size m , $\gamma_{det}(m)/a^2$ for all vacancies, independent of their local environment. Equation (20) needs to be generalized by the addition of two terms,

$$\begin{aligned} \frac{dn_c(m)}{dt} = & n_v(\kappa_v^{m-1}n_c(m-1) - \kappa_v^m n_c(m))D_v/a^2 \\ & + n_i(\kappa_i^{m+1}n_c(m+1) - \kappa_i^m n_c(m))\sqrt{\beta}D_i/a^2 \\ & + (\kappa_d^{m+1}n_c(m+1) - \kappa_d^m n_c(m))\gamma_{det}(m)/a^2 \end{aligned} \quad (23)$$

where κ_d^m represent “detachment numbers” in analogy to the capture numbers $\kappa_{i,v}^m$. Consequently, the condition for detailed balance now reads

$$\begin{aligned} \kappa_v^m n_v n_c(m) D_v / a^2 = & \kappa_i^{m+1} n_i n_c(m+1) \sqrt{\beta} D_i / a^2 \\ & + \kappa_d^{m+1} n_c(m+1) \gamma_{det}(m) / a^2 \end{aligned} \quad (25)$$

and Eq. (22) generalizes to

$$n_c(m) = \frac{\prod_{l=1}^{m-1} \kappa_v^l n_v^l}{\prod_{l=2}^m (\kappa_i^l \alpha \sqrt{\beta} n_i + \kappa_d^l \alpha'(m))}, \quad (26)$$

where $\alpha'(m) = \gamma_{det}(m)a^2/D_v$. We see that the general form of the distribution is the same, but the prefactor changes due to the additional growth and shrinkage probabilities. From a statistical point of view, interstitial arrival and vacancy detachment are equivalent. Eq. (26)

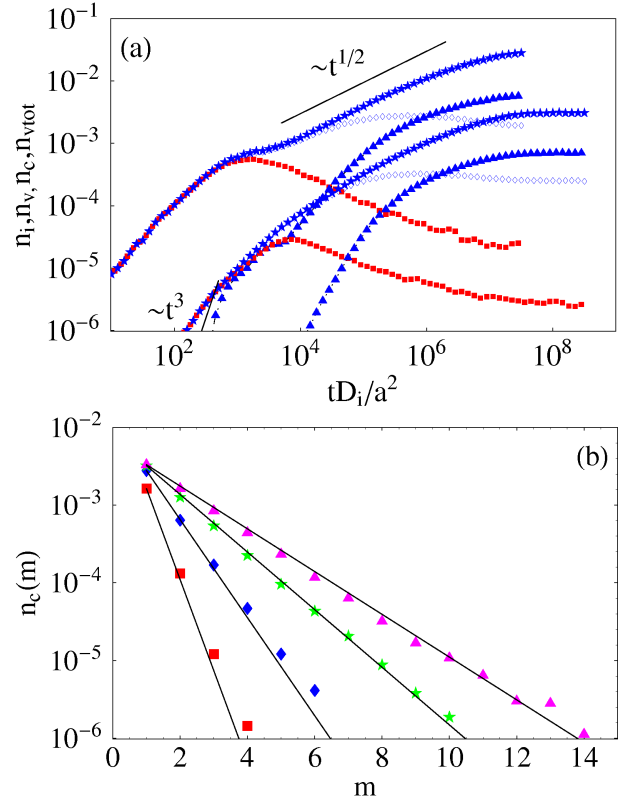


FIG. 4: (a) Interstitial density n_i (■), free vacancy density n_v (◆) as well as the total vacancy density (▲) and vacancy cluster density n_c (★) as a function of time for $\Gamma = 10^5$, and 10^7 for reversible aggregation, where $\delta = 0.01$. (b) Cluster size distribution $n_c(m)$ for the case of $\Gamma = 10^5$ at four different times in Regimes III and IV. The straight lines correspond to $n_v(t)^m / (\alpha\sqrt{\beta}n_i(t) + \kappa_d^1/\kappa_i^1\alpha')^{m-1}$ with $\kappa_d^1/\kappa_i^1 = 0.25$.

can be easily evaluated for any functional form of the size-dependent capture numbers and detachment rates. In the point cluster approximation, where all $\kappa_{i,v,d}^m/\kappa_{i,v,d}^1 = 1$ and $\alpha' = \alpha'(m)$ is size-independent, it predicts an exponential distribution as in the case of irreversible attachment,

$$n_c(m) = \frac{n_v^m}{(\alpha\sqrt{\beta}n_i + \alpha'\kappa_d^1/\kappa_i^1)^{m-1}}. \quad (27)$$

Figure 4 presents a numerical investigation of reversible vacancy cluster growth using kMC. Although detachment rates may be cluster size dependent in general, we only introduce one size-independent rate $\gamma_{det}/a^2 = 0.01D_v/a^2$ for vacancy detachment for simplicity. This model would be most relevant for faceted cluster shapes with one dominant detachment rate from the faces. The other parameters are that of Fig. 2. We see in Fig. 4(a) that the cluster density behaves in a qualitatively similar manner as in the irreversible case, but n_c is reduced and the final steady state is reached at earlier times. As in the irreversible case, the cluster size distribution $n_c(m)$ shown in Fig. 4(b) is well described by Eq. (27). The

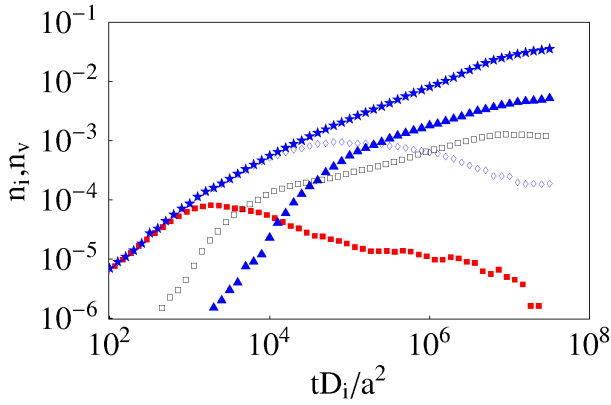


FIG. 5: Interstitial densities n_i (■), free vacancy density n_v (◇), total vacancy density n_{vtot} (▲), vacancy cluster density n_c (★) and density of immobile interstitial cluster (□) as a function of time for $\Gamma = 10^6$.

present discussion is of course only relevant when void coarsening can be neglected.

IV. INTERSTITIAL INTERACTIONS

One of the fascinating aspects of point defect dynamics in bcc metals is the high mobility of interstitial clusters²⁷. The interaction between single interstitial atoms is even stronger than that between vacancies, and the interstitial clusters, such as dislocation loops²⁸, are stable at all relevant temperatures. Unlike the immobile vacancy cluster, however, the interstitial cluster migrate easily for clusters with up to 50 or 100 interstitial atoms^{16,29}. We now modify the preceding analysis to account for this behavior.

In this analysis, we return to the irreversible aggregation limit, i.e., interstitials never separate after encounter. This implies a reduction of the density of mobile interstitials due to nucleation of interstitial clusters, i.e., interstitials act as sinks for other interstitials. However, this creates a population of larger clusters with a larger crosssection and eventually larger capture numbers. The reaction kinetics will be affected by the competition of these two effects.

The rate equations (14) can now be expanded to include terms representing the above processes, but become even more complex. In our kMC model, we begin by studying the effect of interstitial cluster formation by considering completely immobile interstitial clusters in complete analogy to the vacancy cluster. This situation is rarely realistic, but provides an upper bound on the magnitude of the effects. Figure 5 shows the evolution of the free interstitial and vacancy densities as well as the interstitial and vacancy cluster densities for the same parameters as before. As expected, the immobilization of interstitials increases the total number of vacancies in the system. In the final steady state, n_{vtot} is about three times as large as in the situation in Fig. 2. The

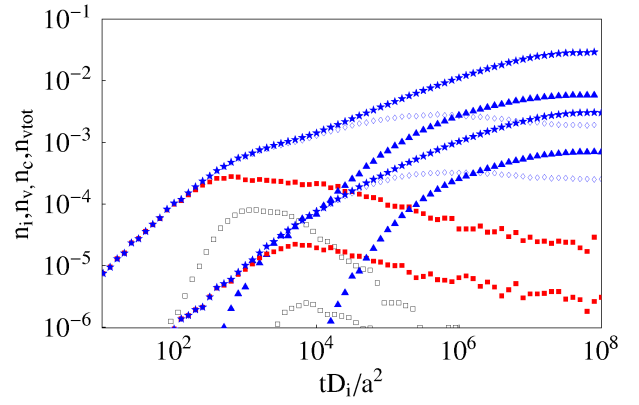


FIG. 6: Interstitial, vacancy, interstitial cluster and vacancy cluster densities for $\Gamma = 10^5$ and $\Gamma = 10^7$ (symbols as in Fig. 5). Interstitial clusters (□) diffuse and rotate with the same rate as single interstitials. The interstitial cluster density first rises due to nucleation events, but then rapidly drops as mobile cluster collide with sinks.

interstitial clusters (open squares) nucleate earlier than the vacancy cluster, but their density later drops below that of the vacancy clusters, since the single interstitial density is much lower than the single vacancy density.

The situation in Fig. 5 can be favorably contrasted with that of completely mobile interstitial clusters, i.e., the cluster diffuse with the same rates as the single interstitials regardless of their size. This case is again not fully realistic, since interstitial clusters seldom rotate into other $\langle 111 \rangle$ directions once they contain several interstitials (i.e., they diffusive one-dimensionally^{29,30}). For small clusters, however, the completely mobile interstitial cluster case represents a good approximation. Figure 6 shows the corresponding results for the various densities introduced above. As in the case of immobile interstitial clusters, the mobile interstitial cluster density first rises due to nucleation events. However, the highly mobile interstitial clusters also collide with the sinks, and the cluster density decreases rapidly. Since the free interstitial density also declines, nucleation events become rare. Once steady state has been achieved, the interstitial density has become so low that the nucleation of new interstitial clusters due to diffusion is almost completely absent. Consequently, the vacancy densities and the total swelling rates are the same as for the case of non-interacting interstitials.

V. APPLICATION TO VANADIUM AND IRON

In this section, we apply our model to the V and α -Fe cases. Vanadium is particularly interesting, because here the effect of mixed 1D/3D diffusion is most pronounced. First principles calculations and classical MD simulations of V have yielded estimates of $\Delta E_i = 0.018\text{eV}^5$, $\Delta E_r = 0.44\text{eV}^5$ and $\Delta E_v \approx 0.5\text{eV}^4$. For Fe, the different ground state of the self-interstitial ($\langle 110 \rangle$ instead of $\langle 111 \rangle$) leads

to a higher effective activation barrier for 1D migration, ΔE_i , which ranges between 0.12 eV³⁰ and 0.17 eV²⁹. The rotation barrier was estimated as $\Delta E_r = 0.16$ eV²⁹, and the vacancy migration energy is assumed to be of the same order¹⁶ as in V (the prefactors for all processes tend to vary by less than an order of magnitude). One therefore expects that the self-interstitial trajectories in α -Fe will be much more isotropic than in V.

The two metals are best compared in terms of the relevant dimensionless parameter α , β and Γ . Table I summarizes the values for these quantities using the above energy barriers and the production rate for ion irradiation $\sigma F = 10^{-3} \text{ s}^{-1}$ for two representative temperatures $T = 300\text{K}$ and $T = 600\text{K}$. We first note that Γ is typically larger than 10^{10} and would in fact reach 10^{20} when typical production rates for neutron irradiation are used. A kMC simulation with such large values of Γ would require very long simulation times, since diffusion and recombination occur much more often than the introduction of new defects. It also requires large system sizes, because the defect densities become very small. In addition, the very small value of β implies very long 1D segments of the interstitial trajectories between rotations. The period of the kMC simulation box should be several times larger than the typical length of those segments in order to properly reproduce the continuum theory values of the encounter rates. If the box period is much smaller than the 1D segment, the trajectory will wrap around the box many times, but is not necessary space-filling.

The last of these issues can be addressed by using a result from Section II, where we showed that the mixed 1D/3D encounter rates scale like the ideal 3D rates that are reduced by a factor $\sqrt{\beta}$. We can therefore replace the explicit 1D/3D trajectories of the interstitials and interstitial cluster with ideal 3D random walks, but reduce the hopping rate by a factor of $\sqrt{\beta}$. This procedure leaves the reaction kinetics invariant (up to small corrections from the capture numbers) and implies that the effective ratio of time scales between interstitial and vacancy migration is given by $\alpha' = D_i \sqrt{\beta} / D_v = \sqrt{D_i \gamma_r / a^2}$. Interestingly, this ratio is very similar for both V and Fe at 300K and 600K (see Table I), even though the values of α and β are very different. At a given temperature, the self-interstitial trajectories in α -Fe are much more isotropic than in V, but the encounter rates with vacancies and sinks only depend on the product of diffusivity

TABLE I: Dimensionless parameters $\alpha = D_i / D_v$, $\beta = \gamma_r / D_i$, $\Gamma = (\sqrt{\beta} D_i + D_v) / \sigma F$, and $\alpha' = \alpha \sqrt{\beta}$ for V and Fe at 300 K and 600 K.

	V-300K	V-600K	Fe-300K	Fe-600K
α	10^8	10^4	10^6	10^3
β	10^{-8}	10^{-4}	10^0	10^0
Γ	10^{11}	10^{13}	10^{11}	10^{13}
α'	10^4	10^2	10^6	10^3

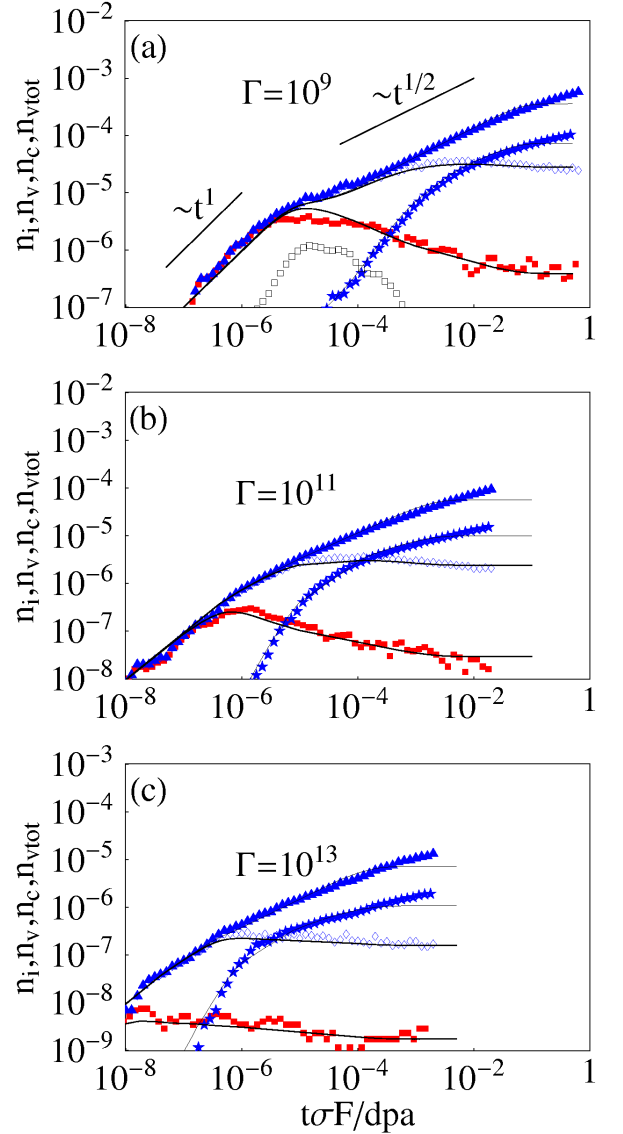


FIG. 7: Interstitial, vacancy, interstitial cluster and vacancy cluster densities (symbols as in Fig. 5) with parameters $\alpha' = 10^2$, $n_s = 10^{-5}$, for (a) $\Gamma = 10^9$ (b) $\Gamma = 10^{11}$ and (c) $\Gamma = 10^{13}$ representative for V or α -Fe at 600K. Thin solid lines show the result of numerically integrating Eqs. (14) again for $\kappa_m = 25$ and $m_{max} = 20$. The solid lines have slope 1 and $1/2$, respectively.

D_i and rotation rate γ_r . Within the present model, one therefore expects that the point defect reaction kinetics in these two metals is very similar.

In Fig. 7, we use a ratio of time scales representative for V/ α -Fe at $T = 600\text{K}$ and show results for $\Gamma = 10^9$, $\Gamma = 10^{11}$ and $\Gamma = 10^{13}$. Here, we have multiplied the time axis with the production rate, which is a more conventional presentation of the data in experimental studies. Rescaled by the production rate, all curves initially coincide and start out with near-constant slopes. For the present parameters, Regime II is practically absent, and the vacancy density crosses over immediately from

Regime I (where it rises linearly with dose) into Regime III. The crossover dose is roughly constant and depends on the sink density. Note that the growth of n_{vtot} in Regime III is well described by a $(\sigma Ft)^{1/2}$ power law over several decades before the final steady-state Regime IV is reached. Since the onset of Regime IV is independent of time (see Section II), larger values of Γ push the beginning of steady state to smaller doses. Here, steady state is reached at about 1 dpa for $\Gamma = 10^9$ and earlier for $\Gamma = 10^{11}$ and $\Gamma = 10^{13}$. There is some initial nucleation of interstitial clusters at $\Gamma = 10^9$, but as discussed before, all of these rapidly disappear due to fast collisions with sinks. For higher values of Γ , the interstitial cluster density becomes negligibly small.

In the same figure, we also show the predictions of a numerical integration of the full set of rate equations (14) using the point cluster model (size independent capture numbers). As in Fig. 2, the agreement with the “exact” kMC simulation is satisfactory. Since the computational effort for direct kMC simulations for $\Gamma > 10^{10}$ becomes tremendous, the rate equation approach, when properly parametrized, is clearly preferable.

VI. CONCLUSIONS

We have studied the early-time evolution of point defect populations with specific reference to migration mechanisms in bcc metals under constant irradiation conditions. Only very simplified models that incorporate the most important processes were employed in order to identify the rate-limiting events. These models were solved using scaling arguments, direct numerical integration of kinetic rate equations and full kMC simulations.

In the simplest case, which only considers homogeneous defect production, recombination and sink absorption, but no interactions between defects of the same type, the kMC model and the corresponding rate equations were shown to be in near perfect agreement. We employed simple random walk arguments to derive a mixed encounter rate that describes one-dimensional diffusion with occasional rotations. This encounter rate scales linearly with target density as the isotropic 3D encounter rate, but is reduced by the square root of the ratio of rotation rate and hopping rate. As in ref. 23, four distinct scaling regimes for the point defect density with time were identified. First, the point defect densities increase linearly in time due to production (Regime I), then saturate as defect recombination sets in (Regime II). Sink absorption then begins to reduce the interstitial density and the vacancy density grows in time with a characteristic $\sim t^{1/2}$ behavior (regime III). A final steady state (Regime IV) is reached when all loss processes are taken into account. The full sequence of Regimes I - IV is most visible when the production rate is not much smaller than the interstitial hopping rates. Regimes II and III shrink with decreasing production rate, and in the limit of very small production rates, Regime I crosses over

directly into Regime IV. These results were based on parameters typical for bcc metals, but the continuum level reaction kinetics equally applies to fcc metals or other crystal structures provided they exhibit similar diffusion mechanisms.

The introduction of vacancy reactions to form immobile vacancy clusters does not change the general sequence of the scaling regimes, but has a profound effect on the population dynamics. In steady state, the density of free vacancies and interstitials is reduced relative to the non-interacting case, but the total number of vacancies n_{vtot} is enhanced. In Regime III, $n_{vtot} \sim t^{1/2}$, and the steady state Regime IV is reached at later times. Reasonable agreement between rate equations and kMC could still be achieved in a point cluster approximation, where the capture numbers are size-independent. Of particular interest is the size distribution of vacancy clusters, which grow and shrink under the diffusive arrival of interstitials and vacancies. For irreversible vacancy aggregation, we derived a new expression for the cluster size distribution, $n_c(m) = \kappa_1 n_v^m / \kappa_m (\alpha \sqrt{\beta} n_i)^{m-1}$. The general form of this distribution remains when also allowing vacancy detachment from the cluster.

Immobile interstitial clusters were shown to further increase the vacancy population. However, interstitial clusters that are as mobile as single interstitials decay rapidly in relevant parameter regimes. We therefore expect that nucleation of interstitial clusters through diffusion plays a negligible role in the microstructural damage evolution of pure bcc metals. It can become important, however, if trapping of self-interstitials near impurities occurs.

Because of their importance in applications and the availability of detailed molecular dynamics studies, we applied the model for parameters suitable for V and α -Fe. Within our model, both metals exhibit similar defect kinetics and therefore similar swelling rates at a given temperature. For production rates and diffusivities in typical experimental situations, our calculations revealed a sequence of growth regimes for the total vacancy density $n_{vtot} \sim t^1$, $\sim t^{1/2}$ and $\sim t^0$. The volume swelling rate follows the same scaling sequence in the sub-1 dpa regime. Interestingly, growth of the vacancy cluster density as $\sim t^{1/2}$ over several decades in time has been observed in the much more detailed kMC simulation of Ref. 16, but the origin of this growth law had not been previously understood. All our simulations reach the steady state regime at damage levels of less than 1 dpa. In the experimentally relevant regime of damage levels between 1 and 100 dpa, it will therefore be more efficient to use steady state rate equations rather than explicit kMC to predict the long time point defect distribution evolution. Nonetheless, it is important to understand the onset of damage evolution and the conditions of applicability of the steady state theory.

The fact that experimental swelling rates of V and α -Fe are very different is of course an indication that our present model does not yet include all relevant phenomena of radiation damage. One obvious refinement

of the models developed here would be a more detailed parametrization of the detachment rates (binding energies) of interstitial and vacancy cluster. However, the intent of the present study has been to focus on general trends rather than quantitative comparisons with experiments, and no new physics is expected to appear from these additional details. For cascade damage conditions³¹, however, two other processes not included in this study are known to have a crucial impact on the defect evolution (in particular void swelling rates). Frenkel pair production is only assumed to be homogeneous for energies right above the displacement threshold, while higher energies lead to the formation of mobile interstitial and immobile vacancy clusters during the cascade phase. Our present model is therefore most relevant to low particle energies. Inclusion of intracascade clustering processes will change results qualitatively and quantitatively, but requires reliable information about the cluster size distribution during cascades from MD

simulations.

In addition to this “production bias”, “absorption bias” also usually exists in bcc metals. “Absorption bias” leads to a preferred absorption of self-interstitials at sinks and is known to be an essential driving force for swelling. The origin of this bias, which leads to increased capture numbers, are long range elastic interactions between point defects and sinks such as dislocations^{32,33} or grain boundaries³⁴. Extensions of the model to include these effects should provide a fruitful topic for future work. The combination of kMC and rate theory can then be used to determine which parameters are most important in radiation damage, so that atomistic simulation resources can be better focused.

The authors gratefully acknowledge useful discussions with L. Zepeda-Ruiz, B. Wirth, and N. Ghoniem as well as the support of the Office of Fusion Energy Sciences (Grant DE-FG02-01ER54628).

-
- ¹ R. A. Johnson and A. N. Orlov, *Physics of radiation effects in crystals* (North-Holland, 1986).
 - ² C. P. Flynn, *Point defects and diffusion* (Clarendon Press, Oxford, 1972).
 - ³ T. Díaz de la Rubia, N. Soneda, M. J. Cartula, and E. A. Alonso, *J. Nucl. Mat.* **251**, 13 (1997).
 - ⁴ S. Han, L. A. Zepeda-Ruiz, G. J. Ackland, R. Car, and D. J. Srolovitz, *Phys. Rev. B* **6**, 220101(R) (2002).
 - ⁵ L. A. Zepeda-Ruiz, J. Rottler, S. Han, G. J. Ackland, D. J. Srolovitz, and R. Car, eprint condmat/0401525 (2004).
 - ⁶ B. D. Wirth, G. R. Odette, D. Maroudas, and G. E. Lucas, *J. Nucl. Mat.* **244**, 185 (1997).
 - ⁷ A. D. Brailsford and R. Bullough, *J. Nucl. Mat.* **44**, 121 (1972).
 - ⁸ C. H. Woo, B. N. Singh, and A. A. Semenov, *J. Nucl. Mat.* **239**, 7 (1996).
 - ⁹ B. N. Singh, S. I. Golubov, H. Trinkaus, A. Serra, Y. N. Osetsky, and A. V. Barashev, *J. Nucl. Mat.* **251**, 107 (1997).
 - ¹⁰ S. I. Golubov, B. N. Singh, and H. Trinkaus, *J. Nucl. Mat.* **276**, 78 (2000).
 - ¹¹ H. Trinkaus, B. N. Singh, and S. I. Golubov, *J. Nucl. Mat.* **283-287**, 89 (2000).
 - ¹² H. L. Heinisch and B. N. Singh, *J. Nucl. Mat.* **232**, 206 (1996).
 - ¹³ H. L. Heinisch and B. N. Singh, *J. Nucl. Mat.* **251**, 77 (1997).
 - ¹⁴ H. L. Heinisch and B. N. Singh, *J. Nucl. Mat.* **271**, 46 (1999).
 - ¹⁵ E. Alonso, M.-J. Caturla, T. D. de la Rubia, and J. M. Perlado, *J. Nucl. Mat.* **276**, 221 (2000).
 - ¹⁶ N. Soneda, S. Ishino, A. Takahashi, and K. Dohi, *J. Nucl. Mat.* **323**, 169 (2003).
 - ¹⁷ T. Iwai, N. Sekimura, and F. A. Garner, *J. Nucl. Mat.* **239**, 157 (1996).
 - ¹⁸ K. Binder and D. W. Heermann, *Monte Carlo Simulations in Statistical Physics* (Springer, Berlin, 1992).
 - ¹⁹ N. Q. Lam, S. J. Rothman, and R. Sizmann, *Rad. Eff.* **23**, 53 (1974).
 - ²⁰ A. D. Brailsford and R. Bullough, *Philos. Trans. R. Soc. London, Ser. A.* **302**, 87 (1981).
 - ²¹ A. V. Barashev, S. I. Golubov, and H. Trinkaus, *Phil. Mag. A* **81**, 2515 (2001).
 - ²² H. Trinkaus, H. L. Heinisch, A. V. Barashev, S. I. Golubov, and B. N. Singh, *Phys. Rev. B* **66**, 060105(R) (2002).
 - ²³ R. Sizmann, *J. Nucl. Mat.* **69/70**, 386 (1968).
 - ²⁴ G. Lück and R. Sizmann, *Phys. Stat. Sol.* **5**, 683 (1964).
 - ²⁵ N. M. Ghoniem, *Phys. Rev. B* **39**, 11810 (1989).
 - ²⁶ J. G. Amar and F. Family, *Phys. Rev. Lett.* **74**, 2066 (1995).
 - ²⁷ Y. N. Osetsky, *Defect and Diffusion Forum* **188-190**, 71 (2001).
 - ²⁸ N. Soneda and T. Díaz de la Rubia, *Phil. Mag. A* **78**, 995 (1998).
 - ²⁹ N. Soneda and T. Díaz de la Rubia, *Phil. Mag. A* **81**, 331 (2001).
 - ³⁰ J. Marian, B. D. Wirth, J. M. Perlado, G. R. Odette, and T. Díaz de la Rubia, *Phys. Rev. B* **64**, 094303 (2001).
 - ³¹ R. Bullough, B. L. Eyre, and K. Krishnan, *Proc. R. Soc. Lond. A.* **346**, 81 (1975).
 - ³² H. Kamiyama, H. Rafii-Tabar, Y. Kawazoe, and H. Matsui, *J. Nucl. Mat.* **212-215**, 231 (1994).
 - ³³ R. Bullough and R. C. Newman, *Rep. Prog. Phys.* **33**, 101 (1970).
 - ³⁴ M. Samaras, P. M. Derlet, H. van Swygenhoven, and M. Victoria, *Phys. Rev. B* **68**, 224111 (2003).